ZNFX1 Functions as a Master Regulator of Epigenetically Induced Pathogen Mimicry and Inflammasome Signaling in Cancer

Lora Stojanovic[1,2], Rachel Abbotts[1,2], Kaushelendra Tripathi[1,2], Collin M. Coon[3], Saranya Rajendran[3], Elnaz Abbasi Farid[3], Galen Hostetter[4], Joseph W. Guarnieri[5], Douglas C. Wallace[5,6], Sheng Liu[7,8], Jun Wan[7,8], Gennaro Calendo[9], Rebecca Marker[2], Zahra Gohari[1,2], Mohammed M. A. Inayatullah[10], Vijay K. Tiwari[10], Tanjina Kader[11,12], Sandro Santagata[11,12,13], Ronny Drapkin[14,15], Stefan Kommoss[16,17], Jacobus Pfisterer[18], Gottfried E. Konecny[19], Ryan Coopergard[20], Jean-Pierre J. Issa[9], Boris J. N. Winterhoff[21], Michael J. Topper[22], George E. Sandusky[23,24], Kathy D. Miller[24,25], Stephen B. Baylin[4,22], Kenneth P. Nephew[3,8,24], and Feyruz V. Rassool[1,2]

ABSTRACT

DNA methyltransferase (DNMT) and PARP inhibitors induce a stimulator of IFN gene–dependent pathogen mimicry response (PMR) in ovarian and other cancers. In this study, we showed that combining DNMT and PARP inhibitors upregulates expression of the nucleic acid sensor NFX1-type zinc finger–containing 1 (ZNFX1) protein. ZNFX1 mediated the induction of PMR in mitochondria, serving as a gateway for stimulator of IFN gene–dependent IFN/inflammasome signaling. Loss of ZNFX1 in ovarian cancer cells promoted proliferation and spheroid formation *in vitro* and tumor growth *in vivo*. In patient ovarian cancer databases, expression of ZNFX1 was elevated in advanced stage disease, and ZNFX1 expression alone significantly correlated with an increase in overall survival in a phase III trial for patients with therapy-resistant ovarian cancer receiving bevacizumab in combination with chemotherapy. RNA sequencing revealed an association between inflammasome signaling through ZNFX1 and abnormal vasculogenesis. Together, this study identified that ZNFX1 is a tumor suppressor that controls PMR signaling through mitochondria and may serve as a biomarker to facilitate personalized therapy in patients with ovarian cancer.

Significance: DNMT and PARP inhibitors induce a nucleic acid sensor, ZNFX1, that serves as a mitochondrial gateway to STING-dependent inflammasome signaling with tumor suppressor properties in ovarian cancer.

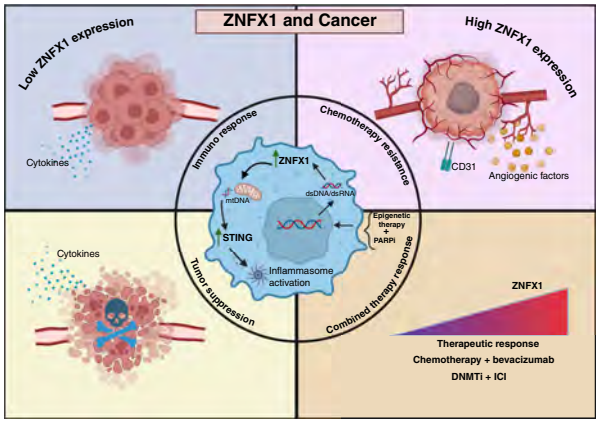

Created in BioRender. Stojanovic, L. (2025) https://BioRender.com/t85w514

Introduction

Anticancer therapies that target epigenetic modulation, such as DNA methylation, induce inflammasome signaling, immune cell attraction, and enhanced efficacy of immune checkpoint therapy (1–4). The DNA methyltransferase inhibitors (DNMTi) 5-azacytidine (AZA) or decitabine (DAC) promote demethylation and transcription of endogenous retroviral elements encoded within the eukaryotic genome, leading to the accumulation of cytosolic double-stranded RNA (dsRNA) transcripts that induce type I IFN (IFNI) signaling (1). Moreover, combining DNMTi with a PARP inhibitor (PARPi) potentiates this effect by inducing IFNI via DNA damage and stimulator of IFN genes (STING)–dependent cytosolic double-stranded DNA (dsDNA) sensor activation, a mechanism we term "pathogen mimicry response" (PMR; refs. 5, 6).

A key gateway for inflammasome signaling is the mitochondria (mt)-mediated defense response (7, 8). Mitochondrial antiviral signaling (MAVS) protein, located in the mt outer membrane, is essential for RIGI-like helicase–mediated antiviral signaling, activating both IFNI transcription via the TBK1–IRF3/7 axis and inflammatory cytokine release via IKK–NF-κB (8). The STING

[1]University of Maryland Marlene and Stewart Greenebaum Comprehensive Cancer Center, Baltimore, Maryland. [2]Division of Translational Radiation Sciences, Department of Radiation Oncology, University of Maryland School of Medicine, Baltimore, Maryland. [3]Medical Sciences Program, Indiana University School of Medicine-Bloomington, Bloomington, Indiana. [4]Van Andel Research Institute, Grand Rapids, Michigan. [5]Division of Human Genetics, Center for Mitochondrial and Epigenomic Medicine, The Children's Hospital of Philadelphia, Philadelphia, Pennsylvania. [6]Division of Human Genetics, Department of Pediatrics, Perelman School of Medicine, University of Pennsylvania, Philadelphia, Pennsylvania. [7]Department of Medical and Molecular Genetics, Indiana University School of Medicine Indianapolis, Indianapolis, Indiana. [8]Department of Anatomy, Cell Biology and Physiology, Indiana University School of Medicine Indianapolis, Indianapolis, Indiana. [9]Coriell Institute for Medical Research, Camden, New Jersey. [10]University of Southern Denmark, Odense, Denmark. [11]Laboratory of Systems Pharmacology, Harvard Medical School, Boston, Massachusetts. [12]Ludwig Center at Harvard, Boston, Massachusetts. [13]Department of Pathology, Brigham and Women's Hospital, Harvard Medical School, Boston, Massachusetts.

pathway, critical for mt involvement in the antiviral immune response (9), activates IFN and NF-κB signaling through detection of dsDNA in the cytosol. Recent evidence shows that viral infection–induced mt dysfunction results in leakage of mitochondrial DNA (mtDNA) into the cytosol and STING-dependent IFN and inflam masome pathway activation, serving as a key mediator of innate immune responses (10, 11). However, the significance of this key process in cancer remains to be established.

A recent report by Vavassori and colleagues (12) describes a rare autosomal recessive deletion of a little-studied protein, NFX1-type zinc finger–containing 1 (ZNFX1) protein, which presents with severe immunodeficiency and multisystem inflammation following viral infection, often leading to death in early childhood. Upon viral infection, ZNFX1 shuttles from the cytosol to the mt outer membrane, where it binds viral dsRNA and interacts with MAVS to increase expression of IFN-stimulated genes (13). In this scenario, ZNFX1 acts as a very early, mt-dependent step for immune activation in defense against viruses (13), but how ZNFX1 mediates these processes is not well understood in general and especially not in cancer.

We now report a master-like role for ZNFX1 as a mediator of mt responses to the presence of dsRNA/dsDNA in the context of DNMTi and PARPi treatment. The combination treatment induces mitochondrial reactive oxygen species (mtROS), mtDNA damage, and subsequent release of damaged mtDNA into the cytosol, culminating in the induction of STING-dependent IFN and inflammasome signaling in ovarian cancer cells. CRISPR knockout (KO) of ZNFX1 in ovarian cancer cells ablates this signaling and reveals tumor suppressor gene–like activity *in vitro* and *in vivo*. Importantly, we show that high ZNFX1 expression alone correlates with a significant increase in overall survival (OS) in patients with recurrent platinum-resistant ovarian cancer receiving the angiogenesis inhibitor bevacizumab, providing the first key evidence for the translational potential of ZNFX1 in cancer.

Materials and Methods

Bioinformatic analysis

Raw The Cancer Genome Atlas (TCGA) counts for ovarian serous cystadenocarcinoma, triple-negative breast invasive carcinoma (TNBC), and colon adenocarcinoma (COAD) were obtained through the Broad Institute GDAC portal. These raw count data were processed using edgeR and Limma-Voom differential expression analyses for RNA sequencing (RNA-seq). For the comparison between ZNFX1 high and ZNFX1 low, samples were split into respective groups based on median normalized count expression. Survival analysis on the ICON7 data was conducted using the survival package in R (14), and significance was determined using a Cox regression followed by a Wald test. Volcano plots were generated using EnhancedVolcano (15). Pathway analyses were conducted using clusterProfiler, an R package for comparing biological themes among gene clusters (16), tidyverse (17), and enrichplot (18). Manually curated dot plots were generated using ggplot2 (19). Microarray expression data were extracted from the Gene Expression Omnibus (GEO) using GEOquery (20), including datasets GSE9891 (21), GSE30161 (22), GSE26193 (23–25). The *Z*-scores of gene expression levels were calculated according to normalization on all genes within samples and then across all samples for the same dataset. Raw counts of genes from the RNA-seq datasets, GSE211669 (26) and GSE102118 (24), were downloaded from the GEO and then converted to fragments per kilobase per million mapped fragments (FPKM) using edgeR (27), followed by *Z*-scores normalized in the same way as microarray expression data. Stage and grade information were retrieved from the GEO and published articles. The Wilcoxon test was conducted to determine statistical significance of differences between stage and grade with regard to ZNFX1 and CMPK2 expression. ZNFX1-KO RNA-seq was conducted as follows: Raw FASTQ files were first assessed for quality metrics using FastQC (28), followed by processing using Trimmomatic (29) to remove adapters and low-quality reads. Processed FASTQ files were then loaded into the Salmon (30) and processed. GENCODE transcript Fasta was used as a transcript reference. Salmon-processed files were used as input for tximport (30), followed by DESeq2 (31) for differential expression analysis. Raw and processed data associated with ZNFX1-KO studies are publicly deposited in GEO.

We used the precancer atlas dataset (please refer to the biorxiv version of the paper: https://www.biorxiv.org/content/10.1101/2024.09.25.615007v1). In brief, we utilized microregional spatial whole-transcriptome (GeoMx; NanoString) dataset described in this study. The specimens were collected from both the incidental group (i.e., no cancer was diagnosed as a part of risk reduction surgeries or opportunistic salpingectomy) and cancer group. We only utilized the regions of the epithelial of the fallopian tube, fimbriae, p53 signature, serous tubal intraepithelial carcinoma (STIC), and cancer. STIC was collected from both incidental and cancer groups. All sample processing and sequencing were performed by the Dana-Farber Sequencing or Harvard Medical School facility. The quality

[14]Department of Obstetrics and Gynecology, Penn Ovarian Cancer Research Center, University of Pennsylvania Perelman School of Medicine, Philadelphia, Pennsylvania. [15]Basser Center for BRCA, Abramson Cancer Center, University of Pennsylvania School of Medicine, Philadelphia, Pennsylvania. [16]Institute for Health Informatics, Diakonie-Klinikum Schwäbisch Hall, Schwäbisch Hall, Germany. [17]Kliniken Essen-Mitte, Gynäkologie und Gynäkologische Onkologie, Essen, Germany. [18]Department of Medicine, David Geffen School of Medicine, Los Angeles, California. [19]University of California Los Angeles, Los Angeles, California. [20]Institute for Health Informatics, University of Minnesota, Minneapolis, Minnesota. [21]Division of Gynecologic Oncology, Department of Obstetrics, Gynecology and Women's Health (OBGYN), University of Minesota, Minneapolis, Minnesota. [22]Department of Oncology, The Sidney Kimmel Comprehensive Cancer Center at Johns Hopkins, Baltimore, Maryland. [23]Pathology and Laboratory Medicine, Indiana University School of Medicine, Indianapolis, Indiana. [24]Indiana University Melvin and Bren Simon Comprehensive Cancer Center, Indianapolis, Indiana. [25]Division of Hematology/Oncology, Department of Medicine, Indiana University School of Medicine, Indianapolis, Indiana.

L. Stojanovic and R. Abbotts contributed equally to the article.

Corresponding Authors: Feyruz V. Rassool, Division of Translational Radiation Sciences, Department of Radiation Oncology, University of Maryland School of Medicine, 655 West Baltimore Street, Baltimore, MD 21201. E-mail: frassool@som.umaryland.edu; Kenneth P. Nephew, Indiana University School of Medicine-Bloomington, 1001 East 3rd Street, Bloomington, IN 47405. E-mail: knephew@iu.edu; and Stephen B. Baylin, Department of Oncology, The Sidney Kimmel Comprehensive Cancer Center at Johns Hopkins, 1650 East Orleans Street, Baltimore, MD 21231. E-mail: sbaylin@jhmi.edu

Cancer Res 2025;85:1183–98

doi: 10.1158/0008-5472.CAN-24-1286

control and the quartile-3 normalization of the initial dataset were performed as suggested by NanoString using GeoMx DSP software, NanoString (v 3.1.0.221). The details of the method and quality control of the data are provided in Materials and Methods and Supplementary Methods of the precancer atlas study.

Pan-cancer bulk RNA-seq analysis

The bulk transcriptome profiles of ZNFX1 were downloaded from the TNMplot database, which utilized datasets from NCBI GEO, Genotype-Tissue Expression (GTex), TCGA, and Therapeutically Applicable Research to Generate Effective Treatments (TARGET) databases (32). For each sample, the transcript read counts were normalized using MAS5 algorithm for NCBI GEO and GTex datasets and using DESeq2 algorithm for TCGA and TARGET datasets to ensure uniform stability in the data.

Cell lines

A2780 and TYK-nu cells (a gift from Dr. Stephen Baylin) were cultured in RPMI-1640 (Corning) supplemented with 10% FBS (Sigma) and 1% penicillin–streptomycin (Sigma). OVCAR4 cells (a gift from Dr. Kenneth Nephew, Indiana University, Bloomington, IN) were cultured in DMEM (Gibco) supplemented with 10% FBS, 1% penicillin–streptomycin, 1% Minimum Essential Medium vitamin solution (Corning), and 1% nonessential amino acids (Corning). The KPCA cell lines were developed and described in Iyer and colleagues (33). Epithelial ovarian cancer cell lines (CP70, A2780, HeyC2, and C272) were maintained in RPMI-1640 (Invitrogen) supplemented with 10% FBS (ATCC) and 1% penicillin–streptomycin solution (ATCC). OVCAR8, OV2008, and HEYA2 cells were maintained in DMEM (Invitrogen) supplemented with 10% FBS (ATCC) and 1% penicillin–streptomycin solution (ATCC). To ensure cell line integrity, all cell lines were thawed at frequent intervals and not used beyond 40 passages. Additionally, cell morphology was monitored for each cell line and proper media and growth conditions selected. All cell lines were cultured at 37°C with 5% CO_2. All cells were regularly tested for *Mycoplasma* contamination.

In vitro treatments

AZA (Sigma) was prepared at 500 μmol/L in PBS. Talazoparib (TAL; BioMarin) was prepared at 5 mmol/L in DMSO. Rotenone (Sigma) was prepared at 10 μmol/L in DMSO. *In vitro* treatments were performed as indicated in the text, with mock treatments performed using an equivalent final concentration of DMSO.

Transfection of the dsDNA mimic polyinosinic:polycytidylic acid or the dsRNA mimic polydeoxyinosinic:deoxycytidylic acid was performed using Lipofectamine 3000 (Invitrogen), followed by a 72-hour incubation.

qRT-PCR

Total RNA was isolated after 3 or 6 days of treatment for qRT-PCR analysis to measure mRNA abundance of the indicated genes, normalized to GAPDH and β-actin mRNAs (**Table 1**). Data presented are the fold change after drug treatment over mock by the ΔΔCT method.

Table 1. Primer sequences used in this study.

Name	Sequence
F-Actin	CACCATTGGCAATGAGCGGTTC
R-Actin	AGGTCTTTGCGGATGTCCACGT
F-GAPDH	GTCTCCTCTGACTTCAACAGCG
R-GAPDH	ACCACCCTGTTGCTGTAGCCAA
F-ERV-K1	ATCCTATGGCACCACCTAGTA
R-ERV-K1	GCCTCAGTATCTCCTTCCTTTC
F-ERVV2	CTTCTTTCTGAGCTCCTGTCTC
R-ERVV2	GTCCTCTGGTTCTTGGTCTTC
F-ERVMER34-1	CCATGGAAGCTCAAGGTCTATC
R-ERVMER34-1	GAAGGGTCCACTGCCATTT
F-ERVW1	CAAGTCCCTTCCCTCTAATTCC
R-ERVW1	TCCACTCCAGCCACTTTAAC
F-ERV-FRD 1	AGCCAGCTCTCAAAGGAAATAG
R-ERV-FRD 1	GAAGGACTACGGCTGCTAAAG
F-ERVW2	CCACTGTCTGTTGGACTTACTT
R-ERVW2	TGGGAGATTGCTTCCTTTACTT
F-ERV-H1	GCCCATTCTCTCTCTCCATATC
R-ERV-H1	CCTGACATTCCTGCCTTCTTA
F-ERVFXA34	CAGGAAACTAACTTTCAGCCAGA
R-ERVFXA34	TAAAGAGGGCATGGAGTAATTGA
F-ERV-Fc1	TACACCCTTACTCCCGTCTT
R-ERV-Fc1	GCCTAACATTCCGACCTCATAC
F-ERV-Fc2	CTGGAAGCTACACACTCCATAC
R-ERV-Fc2	TGCCAAGAGGTGGGTTATTC
F-ERV-Fb1	ATATCCCTCACCACGATCCTAATA
R-ERV-Fb1	CCCTCTGTAGTGCAAAGACTGATA
F-ERV-K8	CCCATCAATCCACCAAGTCTTA
R-ERV-K8	CCTATTTCTTCGGACCTGTTCTT
F-ERV-K10	GTCCCAAGTGTTTCAGGGAATA
R-ERV-K10	GAAGCAGAGAGACTGCTTGTATAG
R-IL18	ACT GGT TCA GCA GCC ATC TT
F-IL18	GGA ATT GTC TCC CAG TGC AT
F-MDA5	GCT GAA GTA GGA GTC AAA GCC C
R-MDA5	CCA CTG TGG TAG CGA TAA GCA G
F-RIG1	CAC CTC AGT TGC TGA TGA AGG C
R-RIG1	GTC AGA AGG AAG CAC TTG CTA CC
F-ZNFX1	GGCAGAGGGAAGAGAGATTTAG
R-ZNFX1	TTCTCCTGGTCATGTCTTTGG
F-MAVS	GTC ACT TCC TGC TGA GA
R-MAVS	TGC TCT GAA TTC TCT CCT
F-CMPK2	TGGAGACCAGGCATCTTAATTT
R-CMPK2	CTCACTGGAACATGATGAGAGG
F-TFAM	GGGAAGGAGGGTTGTGTATTT
R-TFAM	AGGAGTTAGCCAAACGCAATA
F-MT-ATP6	TAGCCCACTTCTTACCACAAGGCA
R-MT-ATP6	TGAGTAGGTGGCCTGCAGTAATGT
F-MT-ND1	CACCCAAGAACAGGGTTTGT
R-MT-ND1	TGG CCATGGGTATGTTGTTAA
F-MT-CO2	AATCGAGTAGTACTCCCGATTG
R-MT-CO2	TTCTAGGACGATGGGCATGAAA
F-MT-D-loop	CTATCACCCTATTAACCACTCA
R-MT-D-loop	TTCGCCTGTAATATTGAACGTA

Immunoblotting

Total cellular protein was extracted in RIPA buffer (Sigma) after 3 or 6 days of treatment. All gels were processed in the same way. In cases when the amount of samples were exceeding the gel capacity, two gels were used side by side, similarly processed, and normalized by the appropriate control. A mitochondrial protein fraction was isolated according to kit protocol (Mitochondrial Isolation Kit, Abcam). The following antibodies were used to determine protein abundance: anti-ZNFX1 (1:1,000, Abcam, #ab179452), anti-MAVS (1:1,000, Abcam, #ab290729), anti-TFAM (1:1.000, Cell Signaling Technology, #8076), anti-VDAC (1:1,000, Cell Signaling Technology, #4866), STAT3 (1:1,000, Cell Signaling Technology, #4904), NF-κB p105/p50 (1:1,000, Cell Signaling Technology, #12540),

NF-κB p65 (1:1,000, Cell Signaling Technology, #8242), pTBK1 (1:1,000, Cell Signaling Technology, #5483), TBK1 (1:5,000, Abcam, #ab40676), STING (1:1,000, Cell Signaling Technology, #13647), pSTING (1:1,000, Cell Signaling Technology, #19781), and vinculin (1:1,000, Cell Signaling Technology, #13907).

Immunofluorescence and proximity ligation assay

Treated cells were plated onto coverslips, fixed in 4% paraformaldehyde, and permeabilized in 0.1% Triton X-100 in PBS.

For immunofluorescence, coverslips were blocked in 10% FBS in PBS and then incubated with the primary antibody against pSTING (rabbit, 1:50, Cell Signaling Technology) and anti-mouse DyLight 594 (Thermo Fisher Scientific). Coverslips were mounted on slides using ProLong Gold antifade reagent with DAPI (4′,6-diamidino-2-phenylindole).

For proximity ligation assay (PLA), coverslips were blocked in 5% goat serum in PBS and then incubated with the primary antibody against ZNFX1 (rabbit, 1:50, Abcam), MAVS (mouse, 1:50, Invitrogen), or dsRNA (mouse, 1:50, EMD Millipore). Duolink *in situ* PLA was performed per the manufacturer's protocols (Sigma), and coverslips were mounted on slides using ProLong Gold antifade reagent with DAPI.

Foci were examined using a Nikon Eclipse 80i fluorescence microscope (100×/1.4 oil).

Detection of reactive oxygen species

Flow cytometric detection of total cellular or mtROS was performed following incubation of cell suspensions for 30 minutes at 37°C with dihydroethidium (3 μmol/L; Invitrogen) or MitoSOX (3 μmol/L, Invitrogen), respectively.

Cytosolic mtDNA detection

Cytosolic fractions were isolated (Mitochondria Isolation Kit for Cultured Cells, Thermo Fisher Scientific) and DNA extracted (QIAamp DNA Blood Mini Kit), according to the manufacturer's protocols. qPCR examining the cytosolic DNA content was performed using primers against mitochondrial (mt-*ATP6*, mt-*CO2*, mt-*ND1*, and D-loop) and nuclear (*GAPDH* and *β-actin*) genes (**Table 1**). Relative cytosolic DNA quantity was normalized against total cellular GAPDH and β-actin mRNAs isolated from the same input samples.

mtDNA damage detection by long PCR

Total cellular DNA was examined by qPCR optimized for the detection of ~8- to 12-kb fragments as previously described (34) using GoTaq Long PCR polymerase (Promega), EvaGreen (1:20 Biotium), and 1× ROX reference dye (Invitrogen). Primers targeted an 8.9-kb-long mitochondrial fragment or 221-bp short mitochondrial reference sequence (**Table 1**). Cycling conditions for long-fragment PCR are as follows: hot start 95°C, 2 minutes; denaturation 95°C, 10 seconds and extension 68°C, 4 minutes 30 seconds (×40 cycles). Cycling conditions for short-fragment PCR are as follows: hot start 95°C, 2 minutes; denaturation 95°C, 10 seconds and extension 60°C, 45 seconds (×40 cycles); and final extension 72°C, 10 minutes.

Detection of cytokine release by ELISA

Cytokine release from the cells were measured in both wild-type (WT) cells and ZNFX1-KO cells in triplicate using ELISA kit according to the manufacturer's protocol. The cells were treated with different concentrations of AZA and TAL, and ELISA was performed. Absorbance was taken at 450 nm using a VersaMax ELISA microplate reader from Molecular Devices. IFNγ was detected by using Invitrogen Human IFN-γ ELISA kit and TNFα detected by using Invitrogen Human TNFα ELISA kit.

8-Hydroxy-2-deoxyguanosine determination using ELISA

mtDNA was isolated from both WT cells and ZNFX1-KO cells, and 8-hydroxy-2-deoxyguanosine was detected using an ELISA kit as described in the manufacturer's protocol. The cells were treated with different concentrations of AZA and TAL, and ELISA was performed. Absorbance was taken at 450 nm using a VersaMax ELISA microplate reader from Molecular Devices. 8-Hydroxy-2-deoxyguanosine was detected using an Abcam human 8-hydroxy-2-deoxyguanosine ELISA kit.

CRISPR-CAS9 KO

CRISPR cell lines exhibiting genetic KO of the *ZNFX1* gene were generated in the Translational Laboratory Shared Services CRISPR Core using the CRISPR-Cas9 mechanism with synthetic single-guide RNAs (Synthego) generated targeting exons 6, 3, 8, and 11 (sequences below). CRISPR-Cas9 KOs were produced by nucleofection on the Lonza Amaxa 4D-Nucleofector platform and confirmed by subjecting cells to PCR and Sanger sequencing. Genomic editing was confirmed by INDEL analysis using the Synthego ICE (Inference of CRISPR Edits) analysis platform. Clonal KO populations were then generated by single-cell plating and screening of clonal sequences using ICE analysis.

Single-guide RNA sequences, human:
Exon 6: ACCCTGGAGTGCACCATGCG
Exon 3: GGAGTGTAACTCTCATGTGA
Exon 8: GCCATGAGGCTAGACCATTG
Exon 11: GGTGGTCCCCAATCAAAATG

mtDNA transfection assays

Total cellular DNA was purified from untreated cells by spin column extraction (Qiagen). mtDNA was PCR-amplified using a REPLI-g Mitochondrial DNA kit (Qiagen) and fragmented using DNase I (New England Biolabs). Fragmented DNA was transfected into cells using Lipofectamine 3000 (Invitrogen). At 72 hours, cellular RNA was collected and assayed by qRT-PCR for expression of IFN-stimulated genes.

Cell doubling

Cells were seeded onto 24-well plates at a density of 50,000 cells/well on day 0 and counted three wells at every 24 hours timepoint using a hemocytometer. The cell number was quantified by plotting the number of cells against period.

Proliferation assay

Cells were seeded into 96-well plates at a density of 500 or 1,000 cells/well and incubated for 2, 4, and 6 days (TYK-nu) or 1, 2, and 3 days (KPCA). Proliferation was assayed using MTS assay (Promega), according to the manufacturer's instructions. Three replicate wells were used for each condition. Absorbance was measured at 490 nm using a spectrophotometer microplate reader.

Transwell migration assay

The transwell migration assay was previously described in (35). In short, Boyden chambers (8 μm pore size; Corning) were placed in the wells of a 24-well plate filled with 750 μL of serum-containing

media which is used as a chemoattractant. A total of 5.0×10^4 cells were suspended in 500 μL of serum-free media, then plated into a Boyden chamber, and allowed to migrate for 16 hours. Following incubation, the medium was aspirated from the Boyden chambers, the internal portion of the membrane washed with PBS and cotton swabs, and the membrane stained with Hema 3 staining kit. The membranes dried for 24 hours before being plated on microscopic slides. Each condition was performed in duplicate, five images were taken per membrane, and cells were counted. Cells were imaged using the 5× objective and counted using ImageJ.

Wound healing

Briefly, cells were counted at a concentration of 5×10^5 cells/mL in cell culture media. The culture insert was aseptically placed at the bottom of a 12-well plate. Approximately 70 μL of cells were added to each side of the insert, and 1 mL of fresh media was introduced into the well surrounding the insert. The cells were allowed to reach a confluent monolayer over 12 to 24 hours in an incubator at 37°C. Prior to commencing the assay, verification of cell confluence inside the insert was conducted. After a 2-hour incubation, the insert was carefully removed to avoid disrupting the cell layer. Media was gently aspirated, and a 1-mL PBS rinse was performed. Fresh media containing 2% FBS was added gently to the side of the well to prevent cell detachment. Cell imaging using a microscope was carried out every 6 hours, capturing at least two images per well. For quantification of the gap area and calculation of the percentage change in area for each cell line or condition, an ImageJ plugin designed for high-throughput image analysis of *in vitro* scratch wound healing assays was utilized.

Colony formation assay

TYK-nu and KPCA cells were plated at a concentration of 1,000 cells/well and 200 or 500 cells/well in a six-well culture plate (Corning), with prewarmed growth media. The cells were evenly dispersed by gently rotating the plate and then incubated for 7 to 10 days. Following the incubation, the cells were fixed with 10% formalin and stained with 0.5% crystal violet in 25% methanol. The plates dried, and the colonies were imaged and counted using Genesys software (Syngene). Each value reported is the mean of three biological replicates, each derived from the mean of three technical replicates (36).

Spheroid assay

Cells were initially seeded at a 60% to 70% confluency level in 10-cm plates. Subsequently, 3,000 cells (TYK-nu) or 1,000 cells (KPCA) were plated in triplicate in 24-well ultralow adherent plates (Corning, cat. #3473) with 1 mL of stem cell medium, following a previously described protocol 3. The cells were allowed to grow for 7 to 10 days. Evaluation of spheroid number and area was conducted using a Zeiss Axiovert 40 inverted microscope equipped with AxioVision software (Carl Zeiss MicroImaging). Spheres or clusters smaller than 100 μm were excluded from the analysis (37).

Cell-cycle analysis

For cell-cycle analyses, approximately 2.5×10^5 cells were plated in a 10-cm dish and allowed to attach overnight. The cells were harvested and fixed overnight in ice-cold 70% ethanol and stored at 20°C until propidium iodide staining. Fixed cells were pelleted, washed in PBS, and incubated with RNase (0.1 mg/mL) at 37°C for 30 minutes. The cells were pelleted again, washed in PBS to remove the RNase, and then resuspended in propidium iodide stain solution (0.1 mg/mL) at a final cell concentration 1×10^6 cell/mL. The cells were then incubated on ice for 30 minutes and analyzed by an LSRII flow cytometry analyzer with FACSDiva software.

Mouse xenograft experiments and IHC

Animal studies were performed under Institutional Animal Care and Use Committee #23-011, and all animals were treated in accordance with the NIH guidelines for laboratory animals and established Institutional Animal Use and Care Committee protocol at the Indiana University, Bloomington. TYK-nu WT and ZNFX1 KO cells (3×10^6 cells) were mixed with Matrigel in a 1:1 ratio and subcutaneously injected into the right flank of NSG female mice. Tumor size was periodically measured using calipers, applying the formula $V = ½ \times L \times W^2$, where L represents the longest tumor diameter and W is the perpendicular tumor diameter. Additionally, body weights were monitored throughout the study. Upon conclusion of the experiment, the mice were euthanized, and the tumors were harvested for subsequent analysis. Tumors excised from mice were fixed overnight in 10% formalin, embedded in paraffin, and sectioned. The sections were stained with hematoxylin and eosin and photographed using a Leica light microscope at ×200 magnification. The sections underwent IHC staining using routine methods. Briefly, sections (5 μm) were deparaffinized, endogenous peroxidase inactivated in 3% peroxide for 10 minutes, and antigen retrieval in 0.1 mol/L sodium citrate performed in a pressure cooker before the sections were blocked with 5% BSA and incubated overnight at 4°C with polyclonal antibodies against ZNFX1, pSTING, pTBX1, WT1, PAX8, and CD34. Primary antibodies were detected using SignalStain Boost Detection Reagent (Rabbit: 8114; Mouse: 8125) and developed with SignalStain DAB Substrate Kit, followed by dehydration with increasing alcohol solutions and mounted. Slides were imaged with Motic EasyScan scanner and analyzed using QuPath software.

Statistical analysis

All data are presented as mean ± SEM with statistical significance derived from the two-tailed unpaired Student t test (or ANOVA).

Data availability

The transcriptomic data analyzed in this study were obtained from TCGA ovarian serous cystadenocarcinoma, TNBC, and COAD cohorts via the Broad Institute GDAC portal (https://gdac.broadinstitute.org/) and GEO at GSE9891, GSE30161, GSE26193, GSE211669, and GSE102118. Bulk transcriptome profiles of ZNFX1 analyzed in this study were downloaded from the TNMplot database (https://tnmplot.com/analysis/), GTEx, and TARGET. Microregional spatial whole-transcriptome data from the precancer atlas dataset were obtained from https://www.biorxiv.org/content/10.1101/2024.09.25.615007v1. The RNA-seq data from ZNFX1-KO TYK-nu cells generated in this study are publicly available in GEO at GSE285444. All other raw data generated in this study are available upon request from the corresponding author.

Results

ZNFX1 expression activates IFN and inflammasome signaling and is linked to mt dysfunction and a tumor suppressor signature

Our analysis of RNA-seq data from multiple cancer databases (TCGA, GEO, GTEx, and TARGET) reveals that ZNFX1 expression is significantly altered in multiple cancers, compared with normal tissue

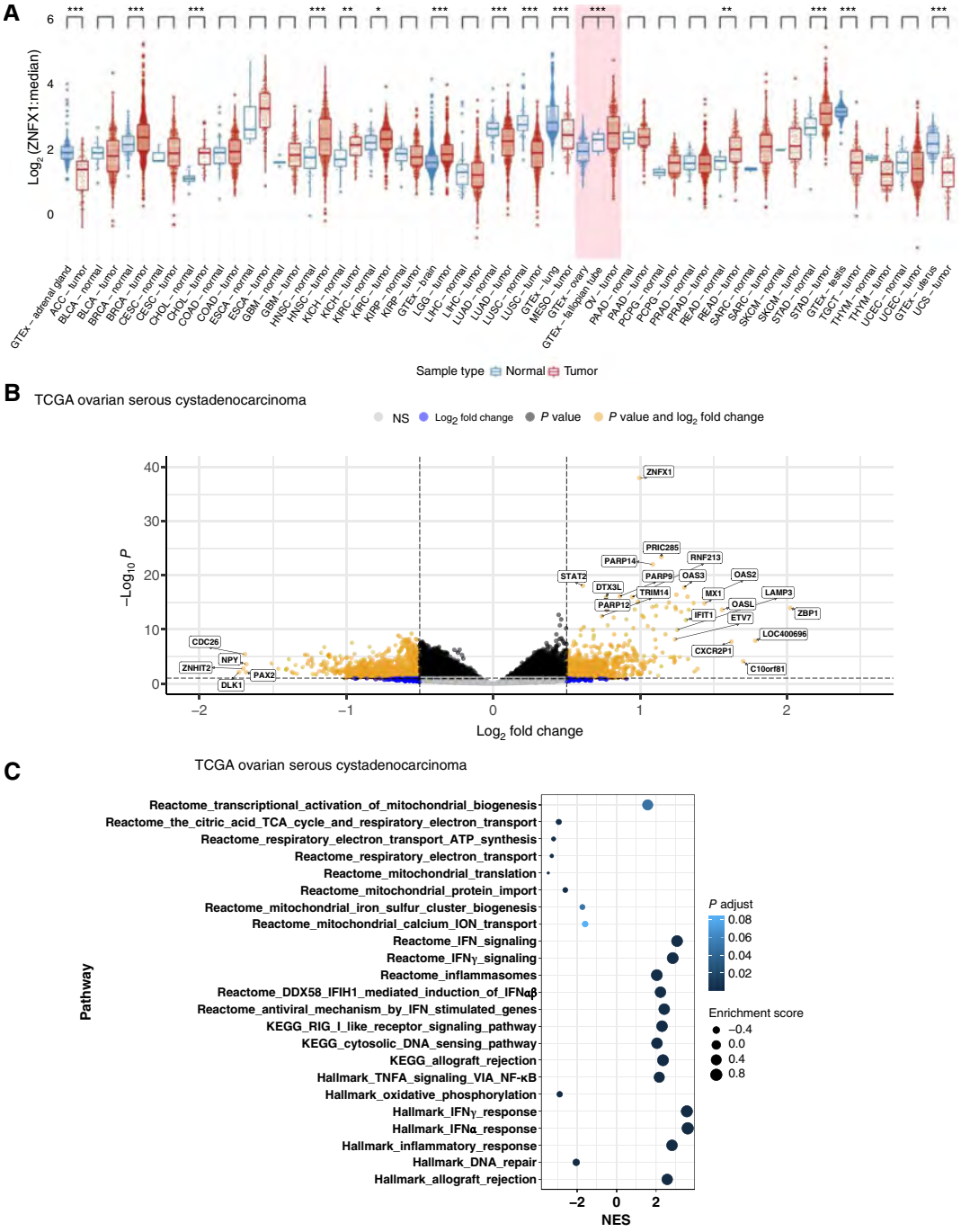

Figure 1.

ZNFX1 expression correlates with IFN/inflammasome signaling but is inversely associated with an mt dysfunction signature in ovarian cancer cells. **A,** Pan-cancer analysis shows significantly higher relative expression of ZNFX1 in ovarian tumors vs. fallopian tube normal samples. Raw RNA-seq expression counts for TCGA and GTEx samples were transformed to $\log_2$ counts-per-million values. The log ratio of ZNFX1 expression to the median expression of all genes in a sample is shown on the *y*-axis for each tissue type. A Wilcoxon rank-sum test was performed on all tumor (red) vs. normal (blue) samples within each tissue type. Unadjusted *P* values (*, $P < 0.05$; **, $P < 0.01$; ***, $P < 0.001$; $P < 0.1$) for each test are shown above each comparison. **B,** Volcano plot for RNA-seq differential expression analysis (TCGA ovarian serous cystadenocarcinoma), all annotated HUGO Gene Nomenclature Committee (HGNC) symbols; *x*-axis, $\log_2$-fold change in expression: ZNFX1 above median vs. ZNFX1 below median; *y*-axis, $-\log_{10}$ of FDR-controlled adjusted *P* value (*P* adj); color mapping, gray, *P* adj > 0.10 and $\log_2$-fold change < |0.5|; black, *P* adj< 0.10 and $\log_2$-fold change < |0.5|; blue, *P* adj> 0.10 and $\log_2$-fold change > |0.5|; orange, *P* adj< 0.10 and $\log_2$-fold change > |0.5|. **C,** Pathway dot plot depicting the result from gene set enrichment analysis (TCGA ovarian serous cystadenocarcinoma) on the preranked gene list derived from ZNFX1 above median vs. ZNFX1 below median differential expression analysis. Pathways depicted are derived from manual curation of IFN, mt, and DNA repair pathways compiled from MSigDB: Hallmark, Kyoto Encyclopedia of Genes and Genomes (KEGG), and Reactome. *x*-axis, normalized enrichment score; dot size, enrichment score; color gradation, FDR-controlled adjusted *P* value. (*Continued on the following page.*)

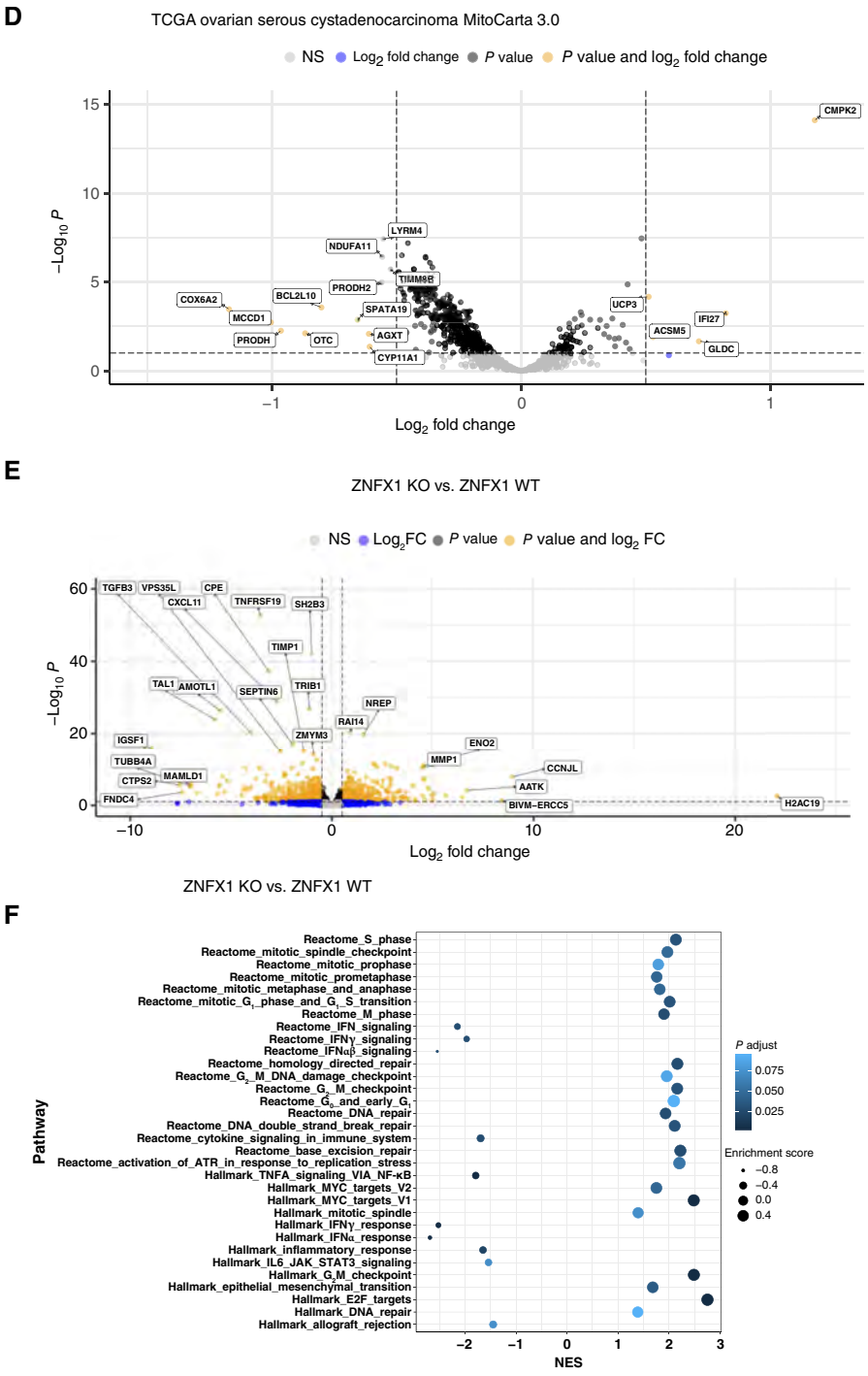

Figure 1.

(*Continued.*) **D,** Volcano plot for RNA-seq differential expression analysis (TCGA ovarian serous cystadenocarcinoma), MitoCarta 3.0 symbols; *x*-axis, $\log_2$-fold change in expression: ZNFX1 above median vs. ZNFX1 below median; *y*-axis, $-\log_{10}$ of FDR-controlled adjusted *P* value (*P* adj); color mapping: gray, *P* adj >0.10 and $\log_2$-fold change < |0.5|; black, *P* adj <0.10 and $\log_2$-fold change < |0.5|; blue, *P* adj >0.10 and $\log_2$-fold change > |0.5|; orange, *P* adj <0.10 and $\log_2$-fold change > |0.5|. **E,** Volcano plot for RNA-seq differential expression analysis (ZNFX1 KO vs. ZNFX1 WT), all annotated HGNC symbols; *x*-axis, $\log_2$-fold change in expression; *y*-axis, $-\log_{10}$ of FDR-controlled adjusted *P* value (*P* adj); color mapping: gray, *P* adj >0.10 and $\log_2$ fold change < |0.5|; black, *P* adj <0.10 and $\log_2$-fold change < |0.5|; blue, *P* adj >0.10 and $\log_2$-fold change > |0.5|; orange, *P* adj <0.10 and $\log_2$-fold change > |0.5|. **F,** Pathway dot plot depicting the result of gene set enrichment analysis on the preranked gene list derived from ZNFX1 KO vs. ZNFX1 WT RNA-seq comparison. Pathways depicted are derived from manual curation of IFN-associated, mt-associated, and DNA repair–associated pathways compiled from MSigDB: Hallmark, KEGG, and Reactome. *x*-axis, normalized enrichment score; dot size, enrichment score; color gradation, FDR-controlled adjusted *P* value.

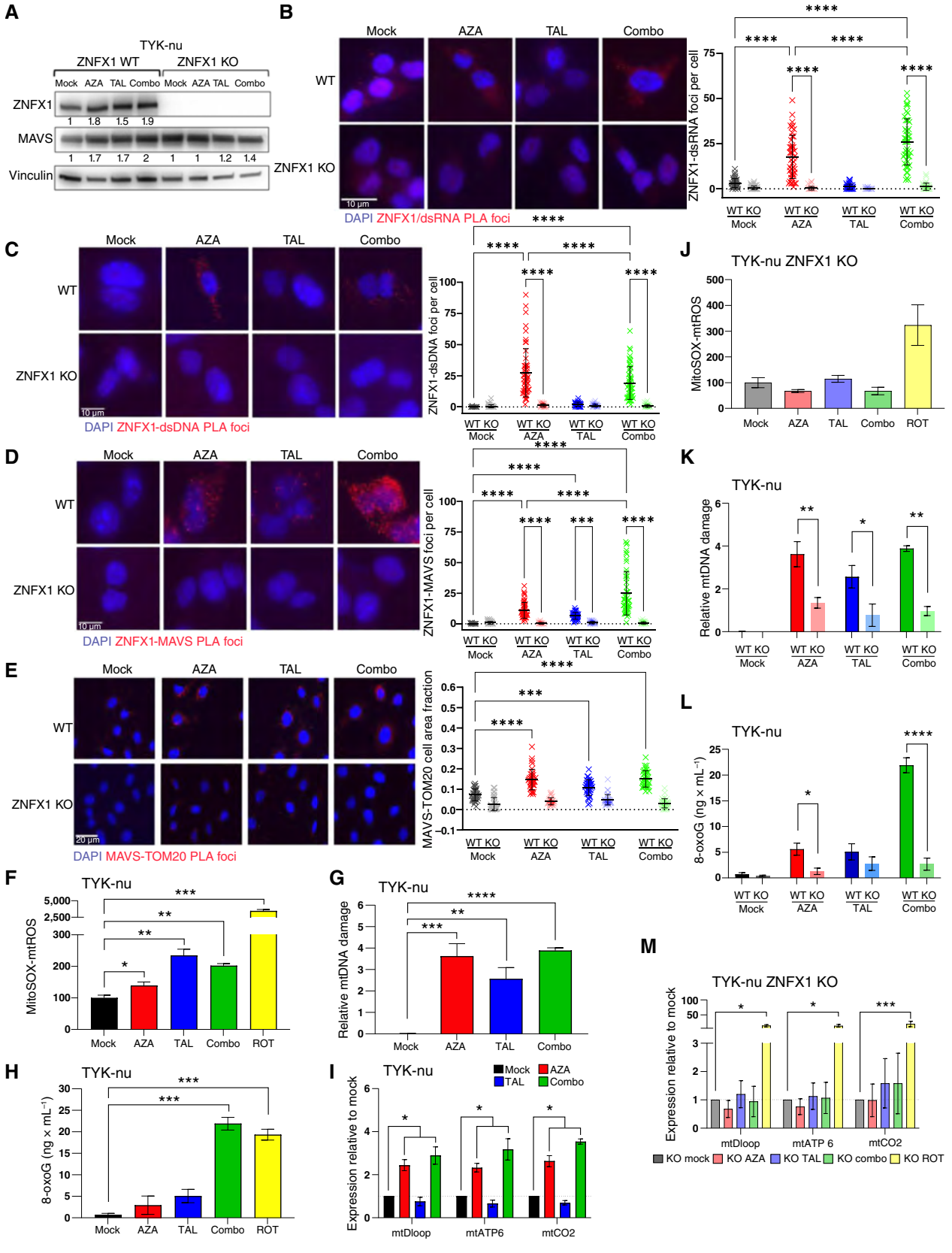

counterparts, including ovarian cancer (**Fig. 1A**; Supplementary Fig. S1A). Genetic alterations in copy number are associated with changes in expression (Supplementary Fig. S1B and S1C). ZNFX1 expression has a positive association with IFN/inflammasome genes mediating innate immune responses, IFN-I and dsDNA/RNA sensing (**Fig. 1B**), but is inversely associated with expression of genes mediating mt function, including metabolism, in MSigDB (**Fig. 1C**; ref. 38) and MitoCarta 3.0 (**Fig. 1D**; ref. 39) databases. Additionally, TCGA analyses in MSigDB (38) and MitoCarta 3.0 (**Fig. 1D**; ref. 39) databases for TNBC (Supplementary Fig. S2A–S2C) and COAD (Supplementary Fig. S3A–S3C) yield similar findings as above. Furthermore, *CRISPR* gene KO of ZNFX1 in BRCA-proficient, high-grade serous ovarian cancer (HGSOC) cell line TYK-nu (Supplementary Fig. S4A) confirms ZNFX1 association with IFN/inflammasome genes and pathways, resulting in 604 downregulated and 443 upregulated differentially expressed genes (**Fig. 1E**). Additionally, gene set enrichment analysis demonstrates the suppression of IFN and inflammasome signaling by ZNFX1 KO (**Fig. 1E** and **F**) and the activation of pathways and expression of leading-edge genes involved in tumorigenesis, including proliferation, migration, and stemness (**Fig. 1E** and **F**; Supplementary Fig. S4B–S4E), which we explore in more detail below. These data suggest that ZNFX1 and IFN/inflammasome signaling correlate with a mt dysfunction and tumor suppressor–like signature in ovarian cancer cells.

ZNFX1 is required for MAVS localization, mt dysfunction, and dsDNA leakage into the cytosol

To expand on the hypothesized role of ZNFX1 as an early PMR defense mechanism for immune activation via mt-mediated mechanisms, we investigated whether ZNFX1 not only binds cytosolic nucleic acids but is crucial for the localization of MAVS to the mt membrane. For these studies, we first show robust ZNFX1 expression in HGSOC in the Cancer Cell Line Encyclopedia database (Supplementary Fig. S5A), validate these studies by using RT-qPCR and Western blot analyses (Supplementary Fig. S5B and S5C), and perform functional assays in TYK-nu, OVCAR4, and A2780 cells. We further show that the transfection of synthetic dsRNA and dsDNA mimics (polyinosinic:polycytidylic acid and polydeoxyinosinic:deoxycytidylic acid, respectively) increases the expression of ZNFX1 (Supplementary Fig. S6A and S6B). Moreover, treatment with the DNMTi AZA alone or in combination with the PARPi TAL mimics this PMR defense mechanism by increasing endogenous retroviral transcription in ovarian cancer cells (Supplementary Fig. S6C), which is in agreement with our previous results in other cancer types (1, 3–5), and associates with an increase in ZNFX1 expression (**Fig. 2A**; Supplementary Fig. S6D). AZA and TAL monotherapies or the AZA–TAL combination increases levels of MAVS (**Fig. 2A**; Supplementary Fig. S6D) and co-localization of ZNFX1 to dsRNA (**Fig. 2B**; Supplementary Fig. S6E), dsDNA (**Fig. 2C**; Supplementary Fig. S6F), and MAVS (**Fig. 2D**; Supplementary Fig. S6G and S6H), as analyzed by PLA and immunofluorescence assay. Importantly, ZNFX1 KO slightly increases MAVS expression with TAL and combination drug treatment but inhibits MAVS co-localization to mt membrane protein TOM20 (**Fig. 2A–E**). Thus, we demonstrate that ZNFX1 binds both dsRNA and dsDNA and plays a crucial role in MAVS localization to the mt outer membrane.

Given that ZNFX1 expression is required for MAVS localization, we hypothesized that ZNFX1 also plays a role in mt dysfunction, as measured by mtROS (11), mtDNA damage, and mtDNA leakage into the cytosol. Transfection of dsDNA/RNA mimics or treatment with AZA, TAL, or AZA–TAL combination markedly increases both mtROS (**Fig. 2F**; Supplementary Fig. S7A–S7C; flow cytometric analysis of specific mtROS dye, MitoSOX) and cellular reactive oxygen species (Supplementary Fig. S7C; dihydroethidium flow cytometric analysis; ref. 36) levels in ovarian cancer cells (23). Moreover, using a long-range PCR for targeting an 8.9-kb-long mt fragment for mtDNA damage as well as ELISA for levels of mt 8-oxoguanine, we show that the above drug treatments increase mtDNA damage (**Fig. 2G** and **H**; Supplementary Fig. S7D–S7F). Finally, PCR analysis for mtDNA in cytosolic extracts demonstrates leakage of mtDNA into the cytosol due to AZA, TAL, or AZA–TAL combination treatments (**Fig. 2I**; Supplementary Fig. S7G and S7H). Importantly, ZNFX1 KO (**Fig. 2A**) abrogates each of these above steps (**Fig. 2J–M**). Taken together, these results support a master role for ZNFX1 in mt dysfunction.

ZNFX1 mediates DNMTi/PARPi-induced STING-dependent IFN/inflammasome signaling

The above dynamics suggest a candidate role for ZNFX1 in AZA-induced and AZA–TAL–induced STING-dependent PMR signaling (5). Accordingly, we show that these treatments (either for 3 or 6 days) induce ZNFX1-dependent increases in IFN/inflammasome gene transcripts and proteins, including TNFα, IFI27, MX2, CCL5, and CXCL10, and these increases are abrogated by knocking out ZNFX1 (**Fig. 3A** and **B**; Supplementary Fig. S8A–S8D). Additionally, forced expression of ZNFX1 (Supplementary Figs. S9A–S9C and S10A) rescues IFN/inflammasome signaling (**Fig. 3C** and **D**; Supplementary Fig. S10B). Likewise, AZA, TAL, or their combination treatment increases levels of STING Ser366 phosphorylation (pSTING, i.e., active STING), as well as downstream pSTING targets pTBK1 and pIRF3 in TYK-nu, OVCAR4, and A2780 cells, and ZNFX1 KO abrogates these increases (**Fig. 3E** and **F**; Supplementary

Figure 2.

DNMTi and PARPi increase ZNFX1 expression, localization with MAVs, and increase mtROS, DNA damage, and dsDNA leakage into the cytosol. The following assays were performed on TYK-nu ovarian cancer cells following 6 days of AZA 100 nmol/L, TAL 2.5 nmol/L, or combination (combo) treatment. **A,** Immunoblotting for ZNFX1 and MAVS. **B–E,** Left, representative immunofluorescence images of ZNFX1 interaction with dsRNA (**B**), dsDNA (**C**), MAVS (**D**), and MAVS and mt membrane protein TOM20 interaction (**E**) by PLA. Right, graphical representation of foci in three independent experiments is plotted. **F,** Flow cytometric detection of MitoSOX measuring mtROS. **G,** Relative mtDNA damage measured by the adapted long-range RT-PCR method. **H,** Relative 8-oxoguanine (8-oxoG) in mtDNA measured by ELISA. **I,** Relative expression of mt-encoded genes (mtDloop, mtATP6/8, and mtCO2) in cytosolic DNA fractions quantitated by qPCR. **J–M,** The following assays were performed on ZNFX1-KO and/or WT TYK-nu ovarian cancer cells following 6 days of treatment with AZA 100 nmol/L, TAL 2.5 nmol/L, or combination. **J,** Flow cytometry detection of mtROS in ZNFX1-KO TYK-nu cells following 6 days of treatment with AZA, TAL, or combination. **K,** Relative mtDNA damage measured by the adapted long-range RT-PCR method in ZNFX1 WT and KO TYK-nu. **L,** Relative 8-oxoG in mtDNA isolated from ZNFX1 KO and WT TYK-nu cells. **M,** Relative expression of mt-encoded genes (mtDloop, mtATP6/8, and mtCO2) in cytosolic fractions isolated from ZNFX1-KO TYK-nu. Rotenone (ROT) was used as the positive control in **F**, **H**, **J**, **I**, and **M**. All data are presented as mean ± SEM, with *P* values derived from the two-tailed unpaired Student *t* test or ANOVA as appropriate. *, $P < 0.05$; **, $P < 0.01$; ***, $P < 0.001$; ****, $P < 0.0001$. All experiments were performed at least three times.

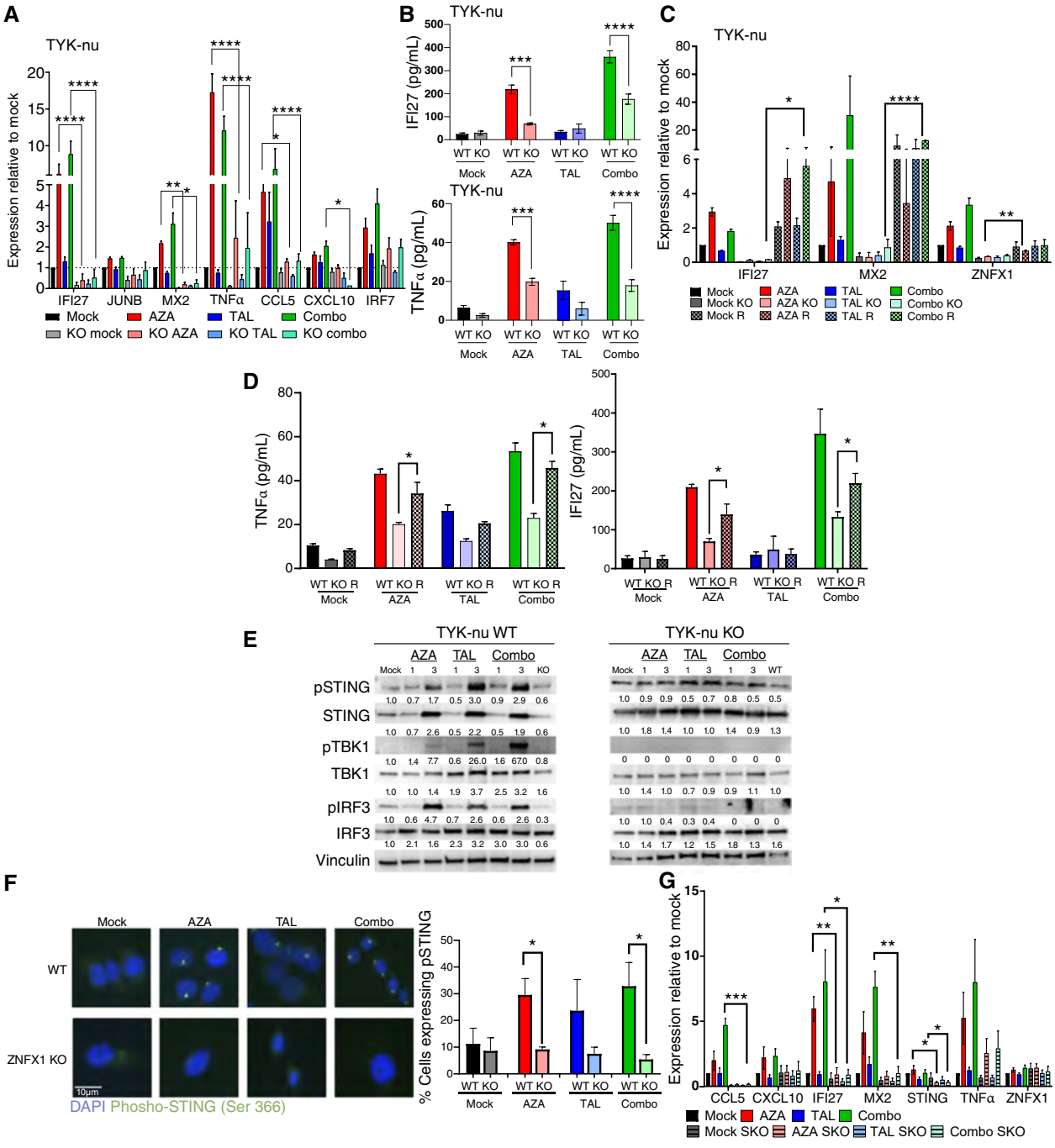

Figure 3.

ZNFX1 increases DNMTi/PARPi-induced STING-dependent IFN and inflammasome signaling, and ZNFX1 KO increases tumorigenic features *in vitro* and *in vivo*. **A,** Relative transcript levels of IFN (IFI27 and MX2) or inflammasome (JUNB and TNFα) by qPCR in TYK-nu ZNFX1 WT or KO following 6 days of treatment with 100 nmol/L AZA, 2.5 nmol/L TAL, or combination. **B,** Levels of cytokines, TNFα (top) and IFI27 (bottom), as measured by ELISA in TYK-nu ZNFX1 WT or KO following 6 days of treatment with AZA 100 nmol/L, TAL 2.5 nmol/L, or combination (combo) in TYK-nu. **C,** Relative transcript levels of IFN (IFI27 and MX2) or inflammasome (JUNB and TNFα) by qPCR in TYK-nu ZNFX1-KO cells transfected with the ZNFX1 plasmid construct following 6 days of treatment with 100 nmol/L AZA, 2.5 nmol/L TAL, or combination. **D,** Levels of cytokines, TNFα (left) and IFI27 (right), as measured by ELISA in TYK-nu ZNFX1-KO cells transfected with the ZNFX1 plasmid construct following 6 days of treatment with AZA 100 nmol/L, TAL 2.5 nmol/L, or combination in TYK-nu. **E,** Relative expression levels of pSTING/STING, pTBKI/TBKI, and pIRF3/IRF3 in protein extracts after 1 and 3 days of treatment with AZA, TAL, and combination in TYK-nu. **F,** Representative immunofluorescence images of Ser366 phosphorylation of STING in TYK-nu ZNFX1 WT or KO following 24 hours of treatment with AZA, TAL, or combination. **G,** Relative transcript levels of STING, IFN (IFI27, MX2, and CCL5), or inflammasome (JUNB and TNFα) by qPCR in TYK-nu STING-KO cells following 6 days of treatment with 100 nmol/L AZA, 2.5 nmol/L TAL, or combination. (*Continued on the following page.*)

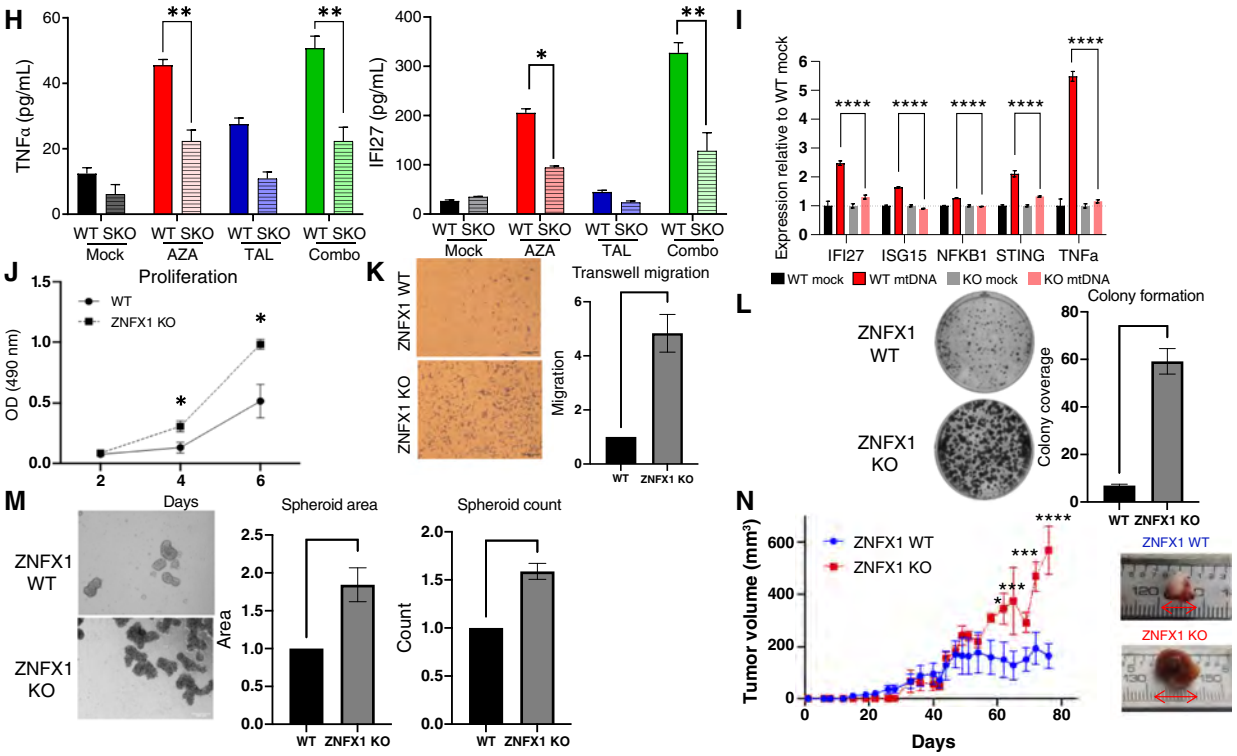

Figure 3.

(*Continued.*) **H,** Levels of cytokines, TNFα (left) and IFI27 (right), as measured by ELISA in TYK-nu ZNFX1 STING KO following 6 days of treatment with AZA 100 nmol/L, TAL 2.5 nmol/L, or combination in TYK-nu. **I,** Relative expression of IFN/inflammasome (IFI27, ISG15, NFKB1, STING, and TNFα) transcripts by qPCR in TYK-nu ZNFX1 WT or KO 72 hours after transfection of purified mtDNA. **J–N,** Effect of ZNFX1 KO on TYK-nu proliferation (seeding density, 500 cells; **J**), migration (**K**), colony formation (1,000 cells/well; **L**), spheroid formation (3,000 cells/well; 7–10 day growth period; **M**), and tumor growth (3×10^6 TYK-nu WT or ZNFX1-KO cells injected subcutaneously; $n = 5$ NSG mice per group; **N**). All data are presented as mean ± SEM, with P values derived from the two-tailed unpaired Student t test or ANOVA as appropriate. *, $P < 0.05$; **, $P < 0.01$; ***, $P < 0.001$; ****, $P < 0.0001$. All experiments were performed at least three times. SKO, STING knockout.

Fig. S11A–S11C). KO of STING has the same effect as ZNFX1 KO (**Fig. 3G** and **H**; Supplementary Fig. S11D and S11E), confirming the effects on STING pathway signaling. The role of mt mediation in the above dynamics is apparent following mtDNA transfection into ZNFX1 WT cells, leading to robust induction of TNFα, NF-κB, IFI27, ISG15, and STING compared with untransfected controls (**Fig. 3I**; Supplementary Fig. S11F). Furthermore, ZNFX1 KO abrogates these changes (**Fig. 3I**; Supplementary Fig. S11F). Taken together, these data support a master role for ZNFX1 in mediating mtDNA induction of STING-dependent IFN/inflammasome signaling.

ZNFX1 KO increases tumorigenic features *in vitro* and *in vivo*

Our RNA-seq data from ZNFX1-KO TYK-nu cells (**Fig. 1D** and **E**) shows the activation of pathways involved in tumorigenesis, including hedgehog signaling pathway genes frizzled class receptor 4 and smoothened (**Fig. 1E**). These data prompted exploring functional analysis of tumorigenesis in ZNFX1-KO cells in human TYK-nu (Supplementary Fig. S12A–S12E) and/or mouse KPCA BRCA-proficient HGSOC cells (Supplementary Fig. S13A–S13J; ref. 33). ZNFX1 KO increases proliferation and decreases cell doubling time (**Fig. 3J**; Supplementary Figs. S12A and S12B, S13B and S13C). Moreover, increases are seen in the rate of wound healing (Supplementary Figs. S12C and S13D) and migration (**Fig. 3K**; Supplementary Fig. S13E), as well as colony (**Fig. 3L**; Supplementary Fig. S13F) and spheroid (**Fig. 3M**; Supplementary Fig. S13G) formation, with no effect on cell-cycle dynamics (Supplementary Figs. S12D and S13H). Importantly, ZNFX1 KO increases tumor growth in xenograft mouse assays (**Fig. 3N**; Supplementary Fig. S12E). Forced expression of ZNFX1 (Supplementary Figs. S9A–S9C and S10A) rescues colony formation (Supplementary Fig. S13J). Knocking out STING induces similar changes in TYK-nu cells (Supplementary Fig. S14A–S14G). IHC analysis of the tumors confirms loss of ZNFX1 in the KO tumors (Supplementary Fig. S15A and S15B) and a trend toward a decrease in p-STING (Supplementary Fig. S15A). In addition, ZNFX1-KO tumors show increased expression of epithelial tumor markers WT1 and CD31, expressed on early and mature vascular endothelial cells (Supplementary Fig. S15B). Collectively, in the context of complete deletion, these functional assays strongly support a tumor suppressor–like role for ZNFX1 in cancer.

Translational significance of ZNFX1 expression

To begin to investigate the translational significance of ZNFX1 in HGSOC, we examined clinical gene expression datasets [Ovarian Cancer Database of Cancer Science Institute Singapore (40) and

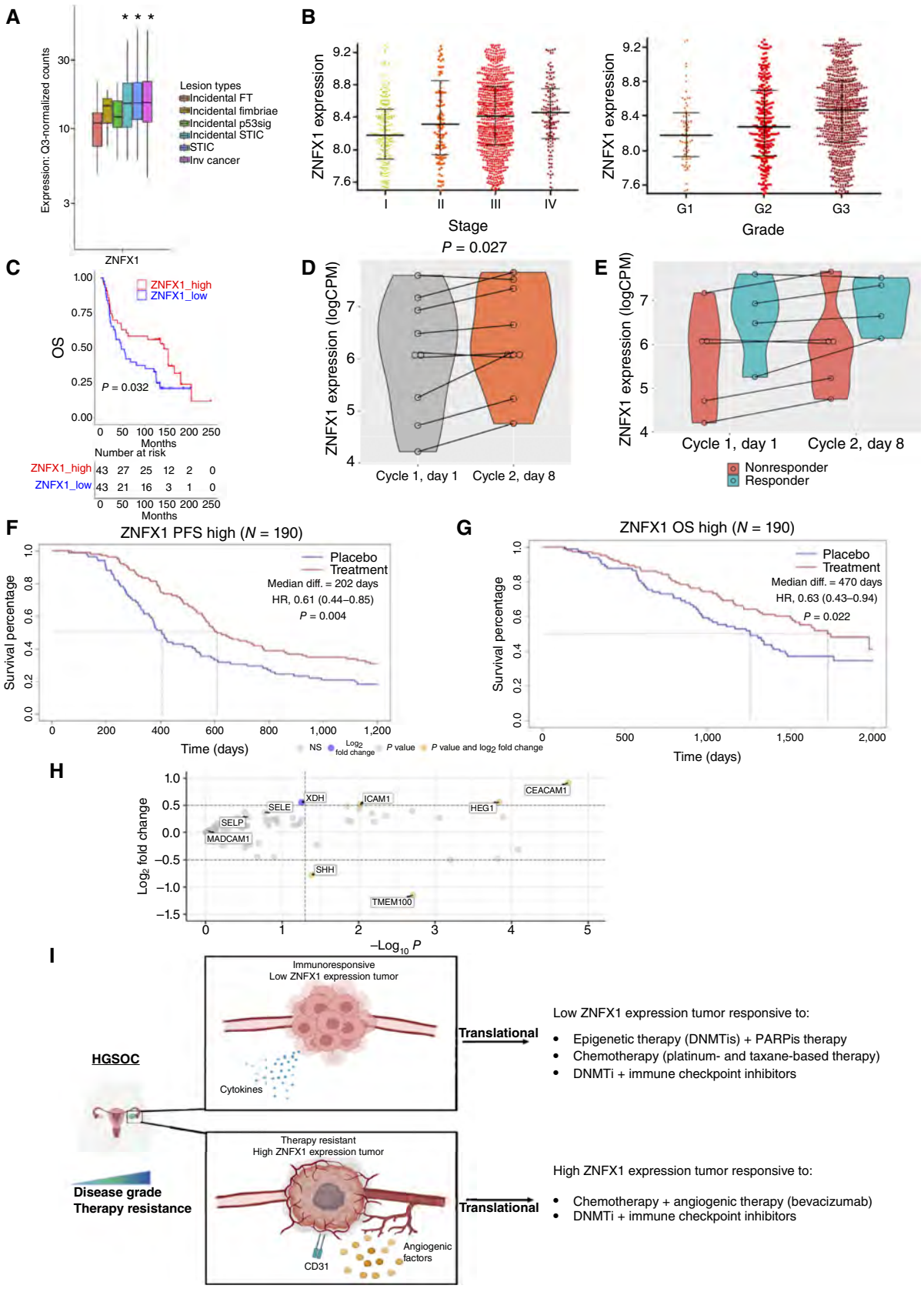

TCGA]. This analysis reveals potentially significant translational findings. First, *ZNFX1* gene expression increases in precursor lesions of HGSOC found in the fallopian tube epithelium (STIC; **Fig. 4A**; ref. 41) and further increases with increasing tumor stage and grade (**Fig. 4B**). Importantly, in the Ovarian Cancer Database of Cancer Science Institute Singapore dataset of 86 patients with HGSOC, high ZNFX1 expression significantly correlates with increased OS ($P = 0.032$; **Fig. 4C**). Second, in support of DNMTis increasing ZNFX1 expression in HGSOC cell lines (**Fig. 2A**), we queried RNA-seq data for pre- and posttreatment tumor biopsies in a phase II clinical trial testing a DNMTi with immune checkpoint therapy in patients with HGSOC (42). In nine available paired samples (pretreatment baseline cycle 1 day 1 versus posttreatment cycle 2 day 8), an increase in ZNFX1 expression is seen in six of the nine patients ($P = 0.027$; **Fig. 4D**). Although n-values for trial outcomes in this small trial allow only a case match to ZNFX1 levels, several interesting relationships emerge: (i) Overall, pretreatment ZNFX1 levels are higher in the four patients with responses (RECIST) than the other patients (**Fig. 4E**); (ii) after DAC treatment, these values remain higher and increase further in two of the four patients (**Fig. 4E**); and (iii) deconvolution studies of the above bulk RNA-seq data demonstrate that when comparing post- versus pre-DAC treatment, the highest versus lowest ZNFX1 quartile levels correlate with statistically significant changes in key immune cell types (CD8, CD4, and plasma B cells; Supplementary Fig. S16A–S16C), in keeping with improved immune responses in some patients in the trial (42).

Finally, and of highest translational significance, we discover that high ZNFX1 expression correlates with outcomes in the ICON7 (43, 44) phase III clinical trial, which tested the anti-VEGF drug bevacizumab added to platinum-based chemotherapy in patients with chemotherapy resistance. This 2011 trial saw an initial increase in progression-free survival (PFS, 3.8 month) but with no improvement in OS. This treatment paradigm (45) is not currently the standard treatment in the United States despite FDA approval (45). Our analysis of *DASL* (cDNA-mediated annealing, selection, extension, and ligation) gene expression data from a subset of the ICON7 trial (43, 44) now shows that low ZNFX1 expression correlates with the significant ($P < 0.002$) improvement of PFS in response to chemotherapy (SF 12) but not with OS [P value = 0.12 (SF12); Supplementary Fig. S17A and S17B]. However, when combined with bevacizumab, high ZNFX1 expression not only significantly correlates with improvement in PFS of 6.6 months but also with a marked significant improvement in OS of 15.6 months (**Fig. 4F** and **G**). To shed light on the above ICON7 findings, our query of the TCGA-OVCA database for gene expression changes associated with high *ZNFX1* gene expression shows that abnormal vasculogenesis tracks with high ZNFX1 expression (**Fig. 4H**). Of particular note, expression of carcinoembryonic antigen–related cell adhesion molecule 1 is a key leading-edge gene change. This immune-inflammasome IRF1-driven gene, when overexpressed in the tumor microenvironment (TME), drives abnormal angiogenesis and immune T-cell tolerance (**Fig. 4H**; ref. 46). Of note, in terms of potential control by ZNFX1 of the above signature, it is reversed in ZNFX1-KO cells with carcinoembryonic antigen–related cell adhesion molecule 1 now the most decreased leading-edge gene (Supplementary Fig. S4E).

Overall, our above data suggest that (i) Increased ZNFX1 expression correlates with increased survival of patients with HGSOC; (ii) DNMTis increase ZNFX1 expression in a clinical setting, with distinct changes in key immune cell subsets; (iii) high ZNFX1 expression in tumors from patients with HGSOC with chemotherapy resistance and accompanying abnormal TME vasculature helps explain why treatment with the anti-angiogenic drug bevacizumab correlate for the first time with significantly increased OS in a subset of ICON7 trial patients (see summary of these points in graphical abstract **Fig. 4I**).

Discussion

Our fundamental finding is that ZNFX1 plays a master regulator role in inducing mt-mediated STING-dependent IFN/inflammasome signaling in ovarian cancer cells. In this paradigm, ZNFX1 is central to MAVS localization and induction of mt dysfunction, previously shown to be important for innate immune responses (7). Our study provides key new insights for how DNMTis and PARPis induce PMR (1–3, 5) and their potential clinical impact as anticancer therapies (47).

Our data indicate that ZNFX1 is activated not only by dsRNA as previously reported (13) but also by dsDNA as well as viral mimics DNMTis and PARPis, culminating in mt dysfunction and leakage of mtDNA into the cytosol, resulting in the activation of STING-dependent IFN and inflammasome signaling. In validation, we also show that transfecting mtDNA in ovarian cancer cells activates STING signaling, whereas the same effect

Figure 4.

Translational relevance of ZNFX1 expression in ovarian cancer. **A,** Box plot depicts the Q3-normalized expression of ZNFX1 in the epithelia with HGSOC progression. The region of interest for each lesion type in *x*-axis was taken from the microregional spatial whole transcriptome (GeoMx). The number of regions of interest per lesion type is as follows: incidental fallopian tube (FT; $n = 29$), incidental fimbriae ($n = 26$), incidental p53 signature ($n = 39$), incidental STIC ($n = 27$), STIC ($n = 96$), and invasive cancer (inv cancer; $n = 105$). *y*-axis is presented in $\log_{10}$ scale. The solid line indicates the median within the IQR, with whiskers extending to a maximum of 1.5 times the IQR beyond the box. Black asterisks indicate significant differences in stages compared with the incidental fallopian tube. *, $P < 0.05$, generalized linear mixed models taking patient ID as random effect. **B,** Expression of ZNFX1 in patients with ovarian cancer in precursor lesions at different tumor stages (left) and grades (right) in the Ovarian Cancer Database of Cancer Science Institute Singapore (CSIOVDB). **C,** OS plotted in CSIOVDB. **D,** Analysis of GSE188249 RNA-seq data (42) for ZNFX1 expression in nine paired samples prior to cycle 1 day 1 and after cycle 2 day 8 (C2D8) epigenetic therapy. **E,** Analysis of RNA-seq data for ZNFX1 expression in samples from responders and nonresponders prior to (cycle 1 day 1) and after (cycle 2 day 8) epigenetic therapy. **F** and **G,** Kaplan–Meier curves for PFS and OS in the ICON7 trial (standard treatment + bevacizumab vs. standard treatment). High vs. low ZNFX1 expression separated by median. **H,** Volcano plot for RNA-seq differential expression analysis of curated vasculogenesis genes from TCGA: ZNFX1 above median vs. ZNFX1 below median, *y*-axis: $-\log_{10}$ of FDR-controlled adjusted *P* value (*P* adj); color mapping: gray, *P* adj >0.10 and $\log_2$-fold change < |0.5|; black, *P* adj <0.10 and $\log_2$-fold change < |0.5|; blue, *P* adj >0.10 and $\log_2$-fold change > |0.5|; orange, *P* adj <0.10 and $\log_2$-fold change > |0.5|. **I,** Graphical summary showing effects of different therapies on basal levels of ZNFX1 as well as tumor responses. Top, HGSOC cells with low basal levels of ZNFX1, DNMTi, and PARPi (**Figs. 2** and **3**), DNMTi and immune checkpoint inhibitors (**E** and **F**), or chemotherapy as in the ICON7 trial (Supplementary Fig. S14) can lead to tumor responses. Bottom, HGSOC cells with high ZNFX1 expression and disease grade and therapy resistance (ICON7 trial data; **G**); cells may also exhibit immune-evasive and angiogenic features that may contribute to responses to chemotherapy plus bevacizumab.

was not observed in ZNFX1-KO cells. Therefore, ZNFX1 could also potentially be mechanistically required for STING activation, suggesting future study of its interaction with STING is warranted. Another mechanism of activating ZNFX1 through mtDNA could potentially involve the direct activation of cGAS (48) in the cytosol as the graphic summary suggests (**Fig. 4I**; Supplementary Fig. S18). Furthermore, IFN-I, dependent on Jak–STAT signaling (13), could also contribute to transcriptional regulation and activation of ZNFX1 in the context of the present study. Regardless of the mechanism involved, once in the cytosol, mtDNA will be detected by ZNFX1 in the similar manner as nuclear DNA and RNA and lead to STING activation.

Our studies also demonstrate that ZNFX1 also acts to suppress cell growth and neoplastic behavior, with tumor suppressor–like properties. Thus, when ZNFX1 is knocked out *in vitro* and *in vivo* in human and mouse ovarian cancer cells, multiple tumorigenic phenotypes emerge. In contrast, when ZNFX1 is chronically expressed at high levels in therapy-resistant cancer cells, antitumor inflammasome signaling can lead to the activation of vasculogenesis-induced immune evasion to enable cancer cell survival. It is now well established that tumors resurrect an embryonic vascular program to escape immunity (49). Blocking such effects in therapy scenarios, as is evident in our trial data for adding bevacizumab to chemotherapy (43, 44), warrants studying the role of ZNFX1 in future basic, clinical, and translational cancer biology investigations.

Our above data have high translational significance in the context of ZNFX1 expression in patients with HGSOC as follows: (i) High ZNFX1 expression tracks with IFN/inflammasome immune signatures in primary HGSOC (TCGA and clinical trial datasets). ZNFX1 levels increase with increasing stage and grade of disease and correlate with overall therapy response (discussed below). (ii) The DNMTi class of epigenetic drugs increases ZNFX1 expression as shown in preclinical studies, which correlates with the known induction of potent immune functions in the TME (47). We now have early *in vitro* evidence of efficacy in HGSOC, which needs rapid translation into a patient-based context to determine the potential synergistic response with immune checkpoint therapies (42). (iii) Perhaps most important, ZNFX1 expression is a potentially robust independent biomarker for predicting therapy responses, per our analysis of a large phase III trial in HGSOC. The majority of patients with HGSOC develop recurrent, chemoresistant disease, limiting 5-year survival, and reversing this resistance is a great unmet need (50). Although the addition of bevacizumab to chemotherapy has shown promise by extending PFS in the ICON7 phase III trial and also in the GOG-218 trial, lack of durability and benefit for OS have prevented this therapy combination from gaining traction in routine HGSOC therapy, despite FDA approval (45). Our finding that high ZNFX1 expression tracks with an impressive increase in the median OS of 15.6 months (**Fig. 4G**), if further validated, suggests that ZNFX1 levels should be considered to personalize the use of bevacizumab in ovarian cancer treatment.

In conclusion, our present findings reveal novel mechanistic and translationally significant roles for the little-studied gene *ZNFX1*. Our studies demonstrate multiple complex properties of ZNFX1 that suggest a master role for controlling mt dynamics, resulting in inflammasome signaling responses to DNMTis and PARPis via STING-dependent IFN/inflammasome induction (1–3, 5, 6). Translationally, levels of ZNFX1 may balance between tumor suppressor functions and immune functions linked to vascular integrity (49). The latter scenario reveals an important biomarker role for ZNFX1 levels in predicting OS for patients with HGSOC receiving bevacizumab therapy.

Authors' Disclosures

D.C. Wallace reports grants from NIH during the conduct of the study, as well as personal fees from Medical Excellence Capital and nonfinancial support from Pano Therapeutics outside the submitted work. S. Santagata reports personal fees from Roche and Novartis and grants from Merck outside the submitted work. R. Drapkin reports personal fees from Repare Therapeutics outside the submitted work. S. Kommoss reports grants and personal fees from GSK and personal fees from AstraZeneca, Eisai, and MSD outside the submitted work. G.E. Konecny reports personal fees from AbbVie, GSK, and AstraZeneca, grants and personal fees from Merck, grants from Eli Lilly and Company, and other support from TORL BioTherapeutics outside the submitted work. B.J.N. Winterhoff reports grants from Adelson Medical Research Foundation during the conduct of the study. K.P. Nephew reports a patent for ZNFX1 as a Biomarker for Ovarian Cancer Therapy and a Predictive Marker for Outcomes in Therapies to Treat Ovarian Cancer pending. F.V. Rassool reports a patent for ZNFX1 as a Biomarker for Ovarian Cancer Therapy and a Predictive Marker for Outcomes in Therapies to Treat Ovarian Cancer pending and issued to University of Maryland, Baltimore (UMB) Ref. Number: FR-2024-066 (PR). No disclosures were reported by the other authors.

Authors' Contributions

L. Stojanovic: Conceptualization, supervision, investigation, writing–original draft, writing–review and editing. **R. Abbotts:** Conceptualization, formal analysis, writing–original draft, writing–review and editing. **K. Tripathi:** Investigation, writing–review and editing. **C.M. Coon:** Investigation. **S. Rajendran:** Investigation, writing–original draft. **E. Abbasi Farid:** Investigation, writing–review and editing. **G. Hostetter:** Validation. **J.W. Guarnieri:** Data curation, formal analysis. **D.C. Wallace:** Writing–review and editing. **S. Liu:** Data curation, formal analysis. **J. Wan:** Data curation, formal analysis. **G. Calendo:** Data curation, software, formal analysis. **R. Marker:** Investigation. **Z. Gohari:** Investigation. **M.M.A. Inayatullah:** Data curation. **V.K. Tiwari:** Data curation. **T. Kader:** Data curation. **S. Santagata:** Data curation. **R. Drapkin:** Data curation. **S. Kommoss:** Data curation. **J. Pfisterer:** Data curation. **G.E. Konecny:** Data curation. **R. Coopergard:** Data curation, software, formal analysis. **J.-P.J. Issa:** Data curation, formal analysis. **B.J.N. Winterhoff:** Conceptualization, writing–review and editing. **M.J. Topper:** Conceptualization, data curation, software, formal analysis. **G.E. Sandusky:** Investigation. **K.D. Miller:** Part of the SPORE project. **S.B. Baylin:** Conceptualization, writing–original draft. **K.P. Nephew:** Conceptualization, formal analysis, writing–original draft, project administration, writing–review and editing. **F.V. Rassool:** Conceptualization, formal analysis, writing–original draft, writing–review and editing.

Disclaimer

The content is solely the responsibility of the authors and does not necessarily represent the official views of the NIH.

Acknowledgments

Our studies were supported by the Adelson Medical Research Foundation (L. Stojanovic, R. Abbotts, M.J. Topper, K. Tripathi, F.V. Rassool, and S.B. Baylin); NCI–Cancer Center Support Grant P30 CA134274 University of Maryland Marlene and Stewart Greenebaum Comprehensive Cancer Center (F.V. Rassool); NIEHS (National Institute of Environmental Health Sciences) grant (2R01ES011858 to R. Abbotts, F.V. Rassool, and S.B. Baylin); NCI grants (1RO1CA259635-01A1; 1RO1AG078814 to D.C. Wallace); the Human Genetics Graduate Program, University of Maryland (L. Stojanovic); the Maryland Department of Health's Cigarette Restitution Fund Program (F.V. Rassool); Specialized Program of Research Excellence program, through NCI grant P50CA254897 (L. Stojanovic, R. Abbotts, K. Tripathi, F.V. Rassool, S.B. Baylin, M.J. Topper, J.-P.J. Issa, and K.P. Nephew); and the Van Andel Research Institute–Stand Up To Cancer Epigenetics Dream Team (S.B. Baylin, F.V. Rassool, and K.P. Nephew). The indicated Stand Up To Cancer grant is administered by AACR, the scientific partner of Stand Up To Cancer. M.J. Topper is a recipient of The Evelyn Grollman Glick Scholar Award. T. Kader, S. Santagata, and R. Drapkin were funded by the Gray Foundation and

Specialized Program of Research Excellence grant (P50CA228991). We thank Dr. Rena Lapidus and Brandon Cooper (University of Maryland Marlene and Stewart Greenebaum Comprehensive Cancer Center, Translational Laboratory Shared Services) for CRISPR-KO studies. We also thank Dr. Aksinijah Kogan for help with R script and bioinformatics early in the project. We also thank Dr. Daniela Matei (Northwestern University). We would like to express our gratitude to the Jerry and Peggy Throgmartin Family for their philanthropic investments in our work.

Note

Supplementary data for this article are available at Cancer Research Online (http://cancerres.aacrjournals.org/).

Received April 18, 2024; revised October 18, 2024; accepted January 7, 2025; published first January 13, 2025.

References

1. Chiappinelli KB, Strissel PL, Desrichard A, Li H, Henke C, Akman B, et al. Inhibiting DNA methylation causes an interferon response in cancer via dsRNA including endogenous retroviruses. Cell 2015;162:974–86.
2. Roulois D, Loo Yau H, Singhania R, Wang Y, Danesh A, Shen SY, et al. DNA-demethylating agents target colorectal cancer cells by inducing viral mimicry by endogenous transcripts. Cell 2015;162:961–73.
3. Topper MJ, Vaz M, Chiappinelli KB, DeStefano Shields CE, Niknafs N, Yen R-WC, et al. Epigenetic therapy ties MYC depletion to reversing immune evasion and treating lung cancer. Cell 2017;171:1284–300.e21.
4. Stone ML, Chiappinelli KB, Li H, Murphy LM, Travers ME, Topper MJ, et al. Epigenetic therapy activates type I interferon signaling in murine ovarian cancer to reduce immunosuppression and tumor burden. Proc Natl Acad Sci U S A 2017;114:E10981–90.
5. McLaughlin LJ, Stojanovic L, Kogan AA, Rutherford JL, Choi EY, Yen R-WC, et al. Pharmacologic induction of innate immune signaling directly drives homologous recombination deficiency. Proc Natl Acad Sci U S A 2020;117:17785–95.
6. Kogan AA, Topper MJ, Dellomo AJ, Stojanovic L, McLaughlin LJ, Creed TM, et al. Activating STING1-dependent immune signaling in TP53 mutant and wild-type acute myeloid leukemia. Proc Natl Acad Sci U S A 2022;119:e2123227119.
7. West AP, Shadel GS, Ghosh S. Mitochondria in innate immune responses. Nat Rev Immunol 2011;11:389–402.
8. Okude H, Ori D, Kawai T. Signaling through nucleic acid sensors and their roles in inflammatory diseases. Front Immunol 2021;11:625833.
9. Kausar S, Yang L, Abbas MN, Hu X, Zhao Y, Zhu Y, et al. Mitochondrial DNA: a key regulator of anti-microbial innate immunity. Genes (Basel) 2020;11:86.
10. Aarreberg LD, Esser-Nobis K, Driscoll C, Shuvarikov A, Roby JA, Gale M Jr. Interleukin-1β induces mtDNA release to activate innate immune signaling via cGAS-STING. Mol Cell 2019;74:801–15.e6.
11. Krysko DV, Agostinis P, Krysko O, Garg AD, Bachert C, Lambrecht BN, et al. Emerging role of damage-associated molecular patterns derived from mitochondria in inflammation. Trends Immunol 2011;32:157–64.
12. Vavassori S, Chou J, Faletti LE, Haunerdinger V, Opitz L, Joset P, et al. Multisystem inflammation and susceptibility to viral infections in human ZNFX1 deficiency. J Allergy Clin Immunol 2021;148:381–93.
13. Wang Y, Yuan S, Jia X, Ge Y, Ling T, Nie M, et al. Mitochondria-localised ZNFX1 functions as a dsRNA sensor to initiate antiviral responses through MAVS. Nat Cell Biol 2019;21:1346–56.
14. Therneau TM. A package for survival analysis in R. R package version 3.5-8; 2024.
15. Blieghe K, Rana S, Lewis M. EnhancedVolcano: Publication-ready volcano plots with enhanced colouring and labeling. https://doi.org/10.18129/B9.bioc.EnhancedVolcano, R package version 1.24.0, https://bioconductor.org/packages/EnhancedVolcano. 2024.
16. Yu G, Wang L-G, Han Y, He Q-Y. clusterProfiler: an R package for comparing biological themes among gene clusters. OMICS 2012;16:284–7.
17. Wickham H, Averick M, Bryan J, Chang W, McGowan LDA, François R, et al. Welcome to the tidyverse. J Open Source Softw 2019;4:1686.
18. Yu G. enrichplot: visualization of functional enrichment result. R package version 1.22.0; 2023.
19. Wickham H. ggplot2: elegant graphics for data analysis. New York (NY): Spring; 2009.
20. Davis S, Meltzer PS. GEOquery: a bridge between the Gene Expression Omnibus (GEO) and BioConductor. Bioinformatics 2007;23:1846–7.
21. Tothill RW, Tinker AV, George J, Brown R, Fox SB, Lade S, et al. Novel molecular subtypes of serous and endometrioid ovarian cancer linked to clinical outcome. Clin Cancer Res 2008;14:5198–208.
22. Ferriss JS, Kim Y, Duska L, Birrer M, Levine DA, Moskaluk C, et al. Multigene expression predictors of single drug responses to adjuvant chemotherapy in ovarian carcinoma: predicting platinum resistance. PLoS One 2012;7:e30550.
23. Furda A, Santos JH, Meyer JN, Van Houten B. Quantitative PCR-based measurement of nuclear and mitochondrial DNA damage and repair in mammalian cells. Methods Mol Biol 2014;1105:419–37.
24. Fang F, Cardenas H, Huang H, Jiang G, Perkins SM, Zhang C, et al. Genomic and epigenomic signatures in ovarian cancer associated with resensitization to platinum drugs. Cancer Res 2018;78:631–44.
25. McCarthy DJ, Chen Y, Smyth GK. Differential expression analysis of multifactor RNA-seq experiments with respect to biological variation. Nucleic Acids Res 2012;40:4288–97.
26. Garsed DW, Pandey A, Fereday S, Kennedy CJ, Takahashi K, Alsop K, et al. The genomic and immune landscape of long-term survivors of high-grade serous ovarian cancer. Nat Genet 2022;54:1853–64.
27. Robinson MD, McCarthy DJ, Smyth GK. edgeR: a Bioconductor package for differential expression analysis of digital gene expression data. Bioinformatics 2010;26:139–40.
28. FastQC. Available from: https://www.bioinformatics.babraham.ac.uk/projects/fastqc/.
29. Bolger AM, Lohse M, Usadel B. Trimmomatic: a flexible trimmer for illumina sequence data. Bioinformatics 2014;30:2114–20.
30. Patro R, Duggal G, Love MI, Irizarry RA, Kingsford C. Salmon provides fast and bias-aware quantification of transcript expression. Nat Methods 2017;14:417–9.
31. Love MI, Huber W, Anders S. Moderated estimation of fold change and dispersion for RNA-seq data with DESeq2. Genome Biol 2014;15:550.
32. Bartha Á, Győrffy B. TNMplot.com: a web tool for the comparison of gene expression in normal, tumor and metastatic tissues. Int J Mol Sci 2021;22:2622.
33. Iyer S, Zhang S, Yucel S, Horn H, Smith SG, Reinhardt F, et al. Genetically defined syngeneic mouse models of ovarian cancer as tools for the discovery of combination immunotherapy. Cancer Discov 2021;11:384–407.
34. Edwards JG. Quantification of mitochondrial DNA (mtDNA) damage and error rates by real-time QPCR. Mitochondrion 2008;9:31–5.
35. Zong X, Wang W, Ozes A, Fang F, Sandusky GE, Nephew KP. EZH2-mediated downregulation of the tumor suppressor DAB2IP maintains ovarian cancer stem cells. Cancer Res 2020;80:4371–85.
36. Pulliam N, Fang F, Ozes AR, Tang J, Adewuyi A, Keer H, et al. An effective epigenetic-PARP inhibitor combination therapy for breast and ovarian cancers independent of BRCA-mutations. Clin Cancer Res 2018;24:3163–75.
37. Wang W, Fang F, Ozes A, Nephew KP. Targeting ovarian cancer stem cells by dual inhibition of HOTAIR and DNA methylation. Mol Cancer Ther 2021;20:1092–101.
38. Liberzon A, Subramanian A, Pinchback R, Thorvaldsdóttir H, Tamayo P, Mesirov JP. Molecular signatures database (MSigDB) 3.0. Bioinformatics 2011;27:1739–40.
39. Rath S, Sharma R, Gupta R, Ast T, Chan C, Durham TJ, et al. MitoCarta3.0: an updated mitochondrial proteome now with sub-organelle localization and pathway annotations. Nucleic Acids Res 2021;49:D1541–7.
40. Tan TZ, Yang H, Ye J, Low J, Choolani M, Tan DSP, et al. CSIOVDB: a microarray gene expression database of epithelial ovarian cancer subtype. Oncotarget 2015;6:43843–52.
41. Kader T, Lin J-R, Hug CB, Coy S, Chen Y-A, de Bruijn I, et al. Multimodal spatial profiling reveals immune suppression and microenvironment remodeling in fallopian tube precursors to high-grade serous ovarian carcinoma. Cancer Discov 2024 Dec 20 [Epub ahead of print]. doi: 10.1158/2159-8290.CD-24-1366.
42. Chen S, Xie P, Cowan M, Huang H, Cardenas H, Keathley R, et al. Epigenetic priming enhances antitumor immunity in platinum-resistant ovarian cancer. J Clin Invest 2022;132:e158800.
43. Perren TJ, Swart AM, Pfisterer J, Ledermann JA, Pujade-Lauraine E, Kristensen G, et al. A phase 3 trial of bevacizumab in ovarian cancer. N Engl J Med 2011;365:2484–96.

44. Kommoss S, Winterhoff B, Oberg AL, Konecny GE, Wang C, Riska SM, et al. Bevacizumab may differentially improve ovarian cancer outcome in patients with proliferative and mesenchymal molecular subtypes. Clin Cancer Res 2017;23:3794–801.
45. Burger RA, Brady MF, Bookman MA, Fleming GF, Monk BJ, Huang H, et al. Incorporation of bevacizumab in the primary treatment of ovarian cancer. N Engl J Med 2011;365:2473–83.
46. Kim WM, Huang Y-H, Gandhi A, Blumberg RS. CEACAM1 structure and function in immunity and its therapeutic implications. Semin Immunol 2019; 42:101296.
47. Topper MJ, Vaz M, Marrone KA, Brahmer JR, Baylin SB. The emerging role of epigenetic therapeutics in immuno-oncology. Nat Rev Clin Oncol 2020;17:75–90.
48. Decout A, Katz JD, Venkatraman S, Ablasser A. The cGAS-STING pathway as a therapeutic target in inflammatory diseases. Nat Rev Immunol 2021;21: 548–69.
49. Huijbers EJM, Khan KA, Kerbel RS, Griffioen AW. Tumors resurrect an embryonic vascular program to escape immunity. Sci Immunol 2022;7: eabm6388.
50. Zhu J, Yan L, Wang Q. Efficacy of PD-1/PD-L1 inhibitors in ovarian cancer: a single-arm meta-analysis. J Ovarian Res 2021;14:112.